Ceramics

CrossMark

Fabrication and characterization of robust freeze-cast alumina scaffolds with dense ceramic walls and controllable pore sizes

Meng-Qi Sun[1], Ping Shen[1,*] , and Qi-Chuan Jiang[1]

[1] *Key Laboratory of Automobile Materials (Ministry of Education), School of Materials Science and Engineering, Jilin University, No. 5988 Renmin Street, Changchun 130022, People's Republic of China*

ABSTRACT

Directionally aligned prismatic and lamellar porous alumina scaffolds with a high strength-to-density ratio were fabricated from submicron Al_2O_3 powders and a tiny quantity of nanoscale TiO_2 sintering aids by freeze casting using TBA and water as solvents. Both freezing temperature (-10 °C, -50 °C, -90 °C) and sintering temperature (1300 °C, 1350 °C, 1400 °C) were varied to adjust pore parameters while a low solid loading (15 vol%) was maintained to ensure high porosity. This paper describes and compares the microstructures, porosity, pore size, wall thickness and compressive behavior of the scaffolds with two typical pore morphologies (lamella and honeycomb), which help to identify their scope of application and to unveil the relationship between pore morphology and mechanical property to optimize the material performance. The failure modes of these two types of scaffolds under compression were simulated. The TBA-based 1 wt% TiO_2-containing alumina scaffolds with dense ceramic walls that were freeze-cast at -90 °C and sintered at 1400 °C exhibited a compressive strength of 160 MPa with a porosity of 59%, indicating lightweight and high-strength characteristics.

Introduction

The design of porous structures that enables the efficient optimization of characteristics such as the strength-to-density and surface-to-volume ratios is desired in aerospace, building, transportation, energy and biomedical industries [1–5]. An ideal porous material should combine mechanical strength with at least one other functional property, such as high permeability, low thermal conductivity or biocompatibility. Generally, sufficient mechanical strength can be associated with a relatively low porosity via mathematical relations, i.e., a power-law or exponential dependence with porosity. However, decreasing the total porosity may degrade other functional properties. Typically, it may degrade the capacity of filtration or ion exchange, or in the case of bone substitutes, it prevents new tissue from

https://doi.org/10.1007/s10853-018-03222-9

growing, which induces loosening and movement of the implant and prevents vascularization and further integration with the body. Therefore, to manufacture robust porous materials with desired levels of open porosity becomes a common challenge that need to be solved.

Porous structures can be obtained by various techniques, such as direct forming, tape casting, slip casting and extrusion [6–10]. In the last decade, freeze casting has emerged as a candidate for preparation of the porous ceramics relying on its simplicity, reliability and especially great flexibility. The high open porosity, good mechanical property, strong anisotropy and fine controllable structure of the resultant scaffolds make it more competitive with traditional techniques. To date, a variety of porous materials fabricated using different powders by freeze casting have indicated their wide application prospects [11–14]. However, only by guaranteeing the sintering quality of ceramics, could freeze casting give full play to its advantages. Usually, in freeze casting, high sintering temperature and long heat preservation time are employed to obtain a certain sintering quality. But they cause high sintering cost, waste of energy and sometimes the change of the original microstructures, which limits their extensive applications in various industrial fields. It is known that adding appropriate sintering aids is a common, cheap and energy-efficient way to reduce the sintering temperature and improve the ceramics mechanical properties. Nevertheless, so far it is rarely reported in the preparation of freeze-cast scaffolds.

As the most common material used in freeze casting, alumina has high inertness which can be used to prepare stable and well-dispersed aqueous slurries with a wide range of solid contents. Freeze-cast alumina scaffolds with different pore morphologies have been fabricated using different solvents [15–19], which show different characteristics and application scopes. However, they are still facing the limitation of high sintering cost and lack of strength-to-density ratio. Adding effective sintering aids might be a promising way to solve these problems. In addition, to improve the combination of properties for the multifunctional applications, it is necessary to consider the influence of pore parameters (e.g., the total volume fraction as well as the shape and size distribution of individual pores). Although the pore morphology has a great influence on the mechanical performance of porous ceramics, it has not received

sufficient attention in freeze casting. From the literature [15–19], we cannot get the clear relationship between pore morphology and mechanical properties because the material, porosity, size and directionality of the resultant materials are notably different.

According to the above background, in this work, we used nanoscale titania as the sintering aids to produce two typical kinds of freeze-cast alumina using water and TBA as the solvents, respectively. The effects of freezing temperature and sintering temperature on the structural parameters of the scaffolds and their compressive property were investigated. Meanwhile, we characterized and compared the microstructures and properties of the freeze-cast alumina with two typical pore morphologies, which would help to identify their scope of application and reveal the relationship between pore morphology and mechanical property.

Experimental procedure

Commercially available powders of Al_2O_3 (VK-L500, Jingrui New Material Co., Xuancheng, China) and TiO_2 (rutile, TBD-R25, Tuoboda Titanium Dioxide Products Co., Wuxi, China) with average particle sizes of 500 nm and 25 nm, and purities of 99.5 wt% and 99.9 wt%, respectively, were used as the raw material and sintering aids. Polyvinyl butyral (PVB, M.W. 40000–70000, Chemical Works, Beijing, China) and citric acid (CA, Chemical Works, Beijing, China) were used as binder and dispersant in conjunction with TBA (chemical purity, Experimental Instruments Co., Dezhou, China) as the solvent, while polyvinyl alcohol and Dolapix Ce 64 (carboxylic acid preparation, Zschimmer & Schwarz GmbH & Co KG Chemische Fabriken, Lahnstein, Germany) were used as the binder and dispersant in conjunction with deionized water as the solvent.

First, alumina slurries were prepared by mixing Al_2O_3 powders in an initial solid loading of 15 vol% and the TiO_2 additive as 1 wt% of the total ceramic powders. The TBA-based slurry was ball-milled for 12 h at 45 °C, and the water-based slurry was ball-milled for 36 h at 25 °C, both using alumina balls. High-quality silicon loop with a good airproof function insured almost no water and TBA lost during ball-milling. Then, the slurries were de-aired by stirring in a vacuum desiccator for 20 min. Subsequently, the slurries were poured into polyethylene

molds with an inner diameter of 18 mm, whose bottom was placed on a Cu bar and top exposed to air. The Cu bar was inserted into liquid nitrogen, and its top surface kept at $-10\ ^\circ C$, $-50\ ^\circ C$ or $-90\ ^\circ C$ by using a ring heater. Therefore, the directional solidification of the slurry from bottom to top was induced. After being frozen, the samples with dimensions of 18 mm in diameter and 30 mm in height were demolded and transferred to a freeze dryer to sublimate the solvent crystals at $-50\ ^\circ C$ under a vacuum of 10 Pa for 48 h. The dried preforms were heated in air at $4\ ^\circ C\ min^{-1}$ to $500\ ^\circ C$, held for 30 min to burn out the organic additives, then heated at a constant rate of $5\ ^\circ C\ min^{-1}$ to a predetermined sintering temperature ($1300\ ^\circ C$, $1350\ ^\circ C$ or $1400\ ^\circ C$), and held for 2 h. Finally, they were cooled at $5\ ^\circ C\ min^{-1}$ to room temperature.

The overall porosity (P) was calculated based on the mass (m) and volume (V) of the samples with respect to the theoretical density (ρ_s) of the fully dense samples ($\rho_{Al_2O_3} = 3.97\ g/cm^3$ and $\rho_{TiO_2} = 4.2\ g/cm^3$; it was assumed that no reaction occurred between Al_2O_3 and TiO_2). Therefore, P can be calculated by using the following equations:

$$P = \left(1 - \frac{m}{\rho_s \times V}\right) \times 100\% \tag{1}$$

$$V = \frac{m_1 - m_2}{\rho_{water}} - \frac{m_1 - m}{\rho_{vaseline}} \tag{2}$$

where m is the mass of the scaffold weighed in air. The total volume of the green body (V) was calculated based on Archimedes' principle (ASTM B962-13). In order to prevent the penetration of deionized water into the porous scaffold, the scaffold was coated with a thin film of vaseline. The mass of the scaffold coated with vaseline measured in air was denoted as m_1. The mass of the vaseline-coated scaffold measured under water was denoted as m_2. ρ_{water} and $\rho_{vaseline}$ are the densities of water and vaseline ($\rho_{water} = 1.0\ g/cm^3$ and $\rho_{vaseline} = 0.84\ g/cm^3$), respectively. The final result was confirmed by measuring at least three samples per condition.

The determinations of porosity, pore size and wall thickness as well as their distributions were performed by image analysis using the "Analyze Particles" and "Local Thickness" plug-in of the Fiji software. To obtain representative values of pore size and wall thickness, we analyzed a minimum of five images per sample. All the images were from cross sections taken perpendicular to the freezing direction (10 mm from the bottom of the sample) with a scanning electron microscope (SEM, VEGA 3 XMU, TESCAN, Czech) and a field emission scanning electron microscope (FESEM, JSM-6700F, Japan). The dimension of the samples after sintering was approximately 25 mm in height. Phase compositions were analyzed by X-ray diffraction (XRD, D/Max 2500PC Rigaku, Japan) with Cu Kα radiation. The compressive strength of the scaffolds was measured by using a universal testing machine (Instron 5689, Instron Corp., USA) at a crosshead speed of $0.18\ mm\ s^{-1}$. The bottom and the top of the samples were removed with a slow-speed diamond saw, leaving the final dimension as approximately 15 mm in height. In all tests, the maximum load at the end of the elastic stage was used to calculate the compressive strength. A minimum of five samples per condition were tested.

Results and discussion

Role of titania in sintering of alumina

The influence of additives on the sintering of alumina is not a new topic. According to references [20–23], as one of the most common sintering aids for alumina, rutile titania (TiO_2) has very similar lattice constants with Al_2O_3 and they can form substitutional solid solution with relatively low melting point during the sintering process, which enhances atomic diffusion and promotes sintering by increasing the lattice defect populations. In order to maintain electrical neutrality, three Ti^{4+} replace out of four Al^{3+} and leave a positive ion vacancy, resulting in an increase in vacancy concentration and diffusion coefficient. The formation of vacancy and lattice distortion can lead to the recrystallization and densification of Al_2O_3 in an effective way. Moreover, the reaction between TiO_2 and Al_2O_3 to form Al_2TiO_5 lowers the sintering activation energy of Al_2O_3. The formation Al_2TiO_5 is associated with the transport of aluminum ions through rutile.

In order to investigate the effect of nano-TiO_2 on the sintering of Al_2O_3, we fabricated the freeze-cast alumina scaffolds with and without 1 wt% TiO_2 under the same processing conditions, respectively. The dimensional evolution of the particles and the microstructures of the TBA-based scaffolds before

and after sintering are shown in Fig. 1. The average particle sizes were estimated from the images using the Fiji software. Before sintering, there is no obvious difference between the scaffolds with and without the sintering aids (Fig. 1a, e). The particles are fine and loosely distributed in the ceramic walls. There are a lot of voids among the particles before sintering. However, with an increase in the sintering temperature, the differences in the particle size and wall density between the scaffolds with and without sintering aids become more and more apparent. Under the same processing conditions, the 1 wt% TiO_2-containing alumina scaffolds (Fig. 1f–h) show thinner ceramic walls, larger sizes of particles and fewer voids as compared with the scaffolds without the sintering aids (Fig. 1b–d).

The total porosity of the scaffolds before and after sintering was tested by the Archimedes method to characterize the densification of the ceramic walls. Note that the grain growth during the sintering process also favors the densification. The removal of porosity and the grain growth occur simultaneously via atomic migration. Therefore, to some extent, the degree of the densification can be reflected by the grain or particle sizes. The average particle size and the porosity in the alumina scaffolds are presented in Fig. 2a, b. In the sample containing 1 wt% TiO_2

sintered at 1400 °C, the average particle size is approx. 3.36 μm, obviously larger than 1.25 μm of the particles sintered at 1300 °C, and more than 7 times the size of the initial Al_2O_3 particles (approx. 437 nm). However, in the sample without the TiO_2 sintering aids, the average particle size of alumina after sintering at 1400 °C is approx. 560 nm, only 1.3 times the size of the initial Al_2O_3 particles and 1/6 that in the counterpart containing 1 wt% TiO_2. On the other hand, the total porosity in the sample containing 1 wt% TiO_2 sintered at 1400 °C is approx. 61%, while the initial porosity in the preform before sintering is 92% (the fact that the porosity of the green body before sintering is larger than the initial solvent content of 85 vol% is due to the volume expansion during the unidirectional solidification of water into ice), and that in the sample sintered at 1400 °C but without the addition of the sintering aids is 85%. The results show that the addition of nano-TiO_2 can significantly accelerate the sintering densification of the freeze-cast alumina scaffolds.

XRD was used to identify the crystalline phases with a step size of 0.06°. As indicated in Fig. 2c, two weak peaks corresponding to TiO_2 and Al_2TiO_5 are identified. The rutile phase exists in the samples sintered from 1300 to 1400 °C. Al_2TiO_5 could be scarcely found in the sample sintered at 1300 °C,
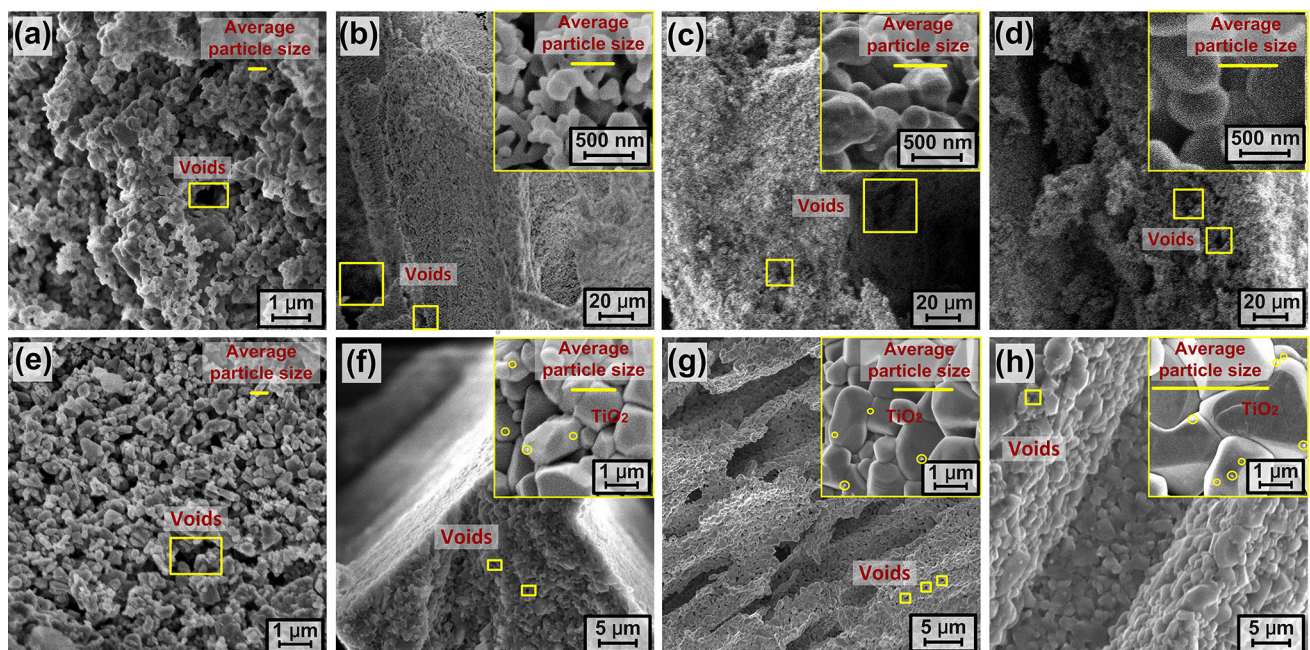

Figure 1 Backscattered FESEM images of alumina architectures **a**–**d** without and **e**–**h** with 1 wt% TiO_2 sintered at different temperatures **a**, **e** 20 °C, **b**, **f** 1300 °C, **c**, **g** 1350 °C and **d**, **h** 1400 °C.
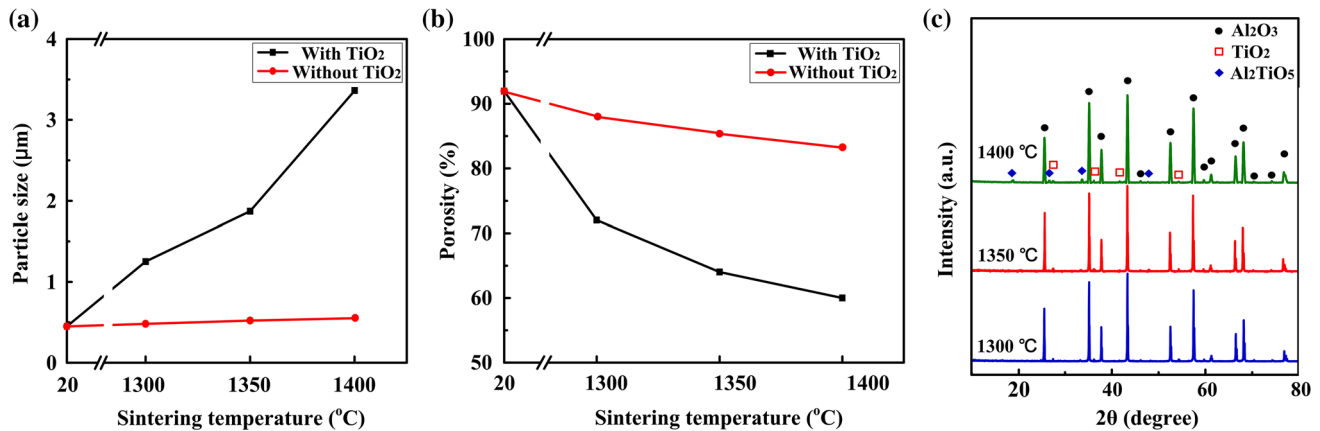
Figure 2 a The average particle size and **b** porosity of the freeze-cast alumina with and without addition of nano-TiO$_2$ as a function of sintering temperature; **c** XRD patterns of the TiO$_2$-containing alumina scaffolds after sintering at different temperatures. The JCPDS file numbers 00-010-0173, 00-021-1276 and 00-041-0258 were used as reference for Al$_2$O$_3$, rutile and Al$_2$TiO$_5$, respectively.

though it could be observed in the samples sintered at 1350 °C and 1400 °C. As we know, TiO$_2$ can react with Al$_2$O$_3$ to form Al$_2$TiO$_5$ when the temperature is above 1280 °C. However, the driving force for the nucleation of Al$_2$TiO$_5$ is too small at 1300 °C, so its quantity is not large enough to be identified after sintering at 1300 °C. The presence of rutile and Al$_2$TiO$_5$ phases may bring a strengthening effect for alumina. As mentioned above, the addition of TiO$_2$ could lead to enhanced densification of Al$_2$O$_3$ during high-temperature sintering. This behavior could contribute to the strength of the freeze-cast scaffolds. In addition, some studies indicated that the increase in the residual stress due to the mismatch of thermal expansion coefficients between Al$_2$O$_3$ and Al$_2$TiO$_5$ may improve the compressive strength of Al$_2$O$_3$ [24].

Microstructures of the ceramic architectures

The SEM images of typical microstructures perpendicular (Fig. 3a, c) and parallel (Fig. 3b, d) to the freezing direction show views of the unidirectionally aligned pore channels, which are replicas of TBA (Fig. 3a, b) and ice crystals (Fig. 3c, d), respectively. According to the crystal structure of TBA, the TBA-based scaffolds provide approximately hexagonal pore channels with isotropy perpendicular to the freezing direction. As we know, TBA contains three symmetry-independent molecules, and they form six-membered rings with six hydrogen bonds forming each ring, as shown in Fig. 3e. The crystal packing of these hexamers presents a hexagonal layer. Within one layer, the growth of crystals shows isotropic

characteristics. Between these layers, the hexamers are linked by methyl–methyl contacts, which form nearly ideal equilateral triangles. Under unidirectional freezing conditions, TBA solidifies in the form of chains, subsequently leaving unidirectionally aligned pore channels after sublimation. Different from TBA, water transforms to lamellar ice crystals with anisotropy perpendicular to the freezing direction. This can be understood with reference to the basic crystallographic and crystal growth characteristics of ice. Ice nucleates first as a form of small hexagonal structures that contain hydrogen bonds between water molecules, as shown in Fig. 3f. With the progress of crystallization, the ice front velocity parallel to the crystallographic c axis is 10^2–10^3 times slower than that perpendicular to the c axis because the water molecules preferentially adhere to the rough interface rather than forming a new interface on the other side. The ice crystals become larger to form lamellae via the two-dimensional growth of hexagonal structures with a rich in-plane structure having a hexagonal symmetry until the growth of crystals in the b-axis direction is confined by ceramic particles which are squeezed by adjacent ice crystals. Then, the crystals keep growing in the a-direction, leaving unidirectionally aligned pore channels after sublimation.

From Fig. 3, we can see that both these two kinds of pores are distributed homogeneously within the location. Different from the two-dimensional isotropic prismatic pores, the anisotropic lamellar pores align locally and orient to different directions as marked by yellow arrows 1 and 2 in Fig. 3c. In the
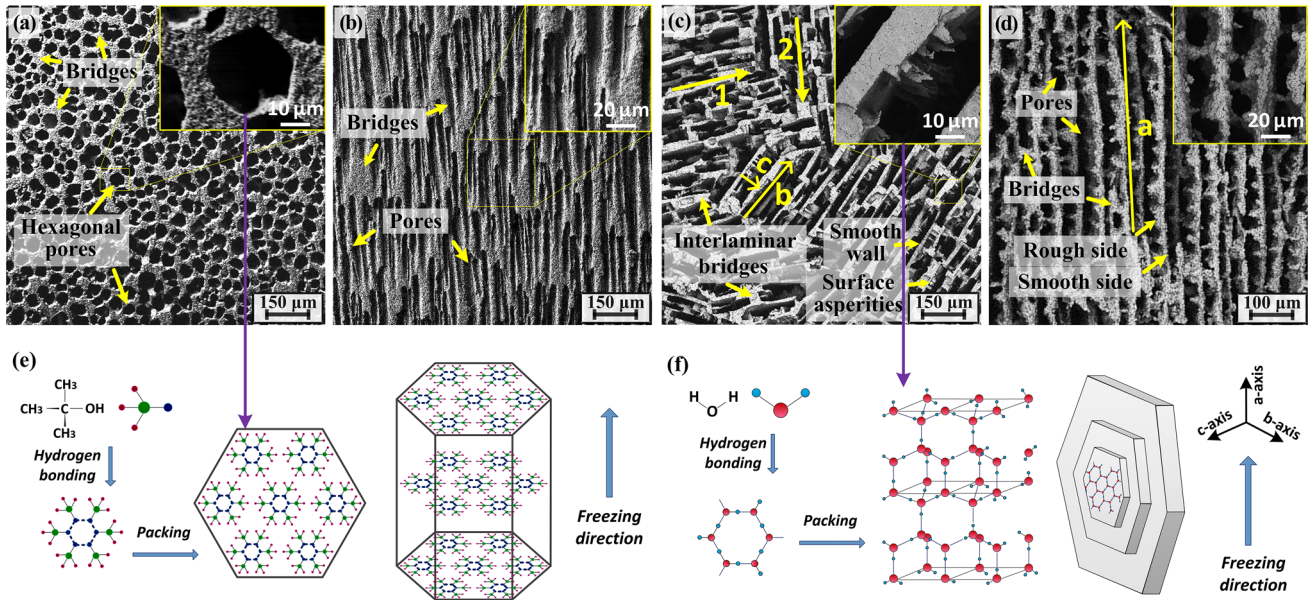
Figure 3 Typical SEM micrographs of porous 1 wt% TiO_2-containing alumina prepared from different solvents: **a**, **b** TBA and **c**, **d** H_2O (Both of them were freeze-cast at − 10 °C and sintered at 1400 °C; **a**, **c** perpendicular to the freezing direction; **b**, **d** parallel to the freezing direction); **e** the molecular structure and the hexamerous crystal structure of TBA under unidirectional freezing conditions; **f** the molecular structure of water and the ice crystal growth behavior under unidirectional freezing conditions.

whole field of view, the arrangement of prismatic pores is more ordered than that of lamellar pores. Moreover, a large number of robust and uniformly distributed bridges in the TBA-based scaffold make all walls interconnected closely, like a two-dimensional network. However, in the water-based scaffold, the sparse bridges form lap joints between ceramic walls and the connection between layers are relatively loose. In addition, the ceramic walls in the TBA-based scaffold are smooth while numerous surface asperities exist in the water-based scaffolds. Also, the surface asperities usually locate on one side of pore channels, while the other side is planar due to the non-overlapping directions of ice growth [16].

Wall thickness and pore size distribution

The honeycomb and lamellar microstructures of 1 wt% TiO_2-containing alumina obtained via the freeze-casting process can be finely tailored on a large scale by changing either the freezing temperature or the sintering temperature. Figure 4 shows SEM images of typical transverse sections perpendicular to the freezing direction of the honeycomb (Fig. 4a–e) and lamellar (Fig. 4f–j) scaffolds obtained at different freezing temperatures (− 10 °C, − 50 °C, − 90 °C) and sintering temperatures (1300 °C, 1350 °C,

1400 °C). The samples are all chosen from the same location, approximately 10 mm from the bottom to ensure uniform vertical wall thickness without large variations. Clearly, when the freezing temperature is constant (Fig. 4a–c, f–h), both the pore size and wall thickness decrease with an increase in the sintering temperature due to the positive correlation between sintering temperature and volume shrinkage ratio. When the sintering temperature is constant, both the pore size and wall thickness decrease with the freezing temperature. It can be explained by the nucleation theory. The higher undercooling degree ahead of the ice front induced from faster cooling velocity results in a larger nucleation rate. The more crystal nuclei in the ceramic slurry yield the thinner pore size and the smaller wall thickness in the sample under the restriction of ceramic particles which were squeezed by adjacent crystals.

The wall thickness and pore size distributions are presented in Fig. 5, which were determined by image analysis using the "local thickness" plug-in of the Fiji software. The results show that lower freezing temperatures and higher sintering temperatures are more beneficial for generating uniform wall thickness and pore size distributions and fine structures. Within the certain range of freezing temperature (from − 10 to − 90 °C) and sintering temperature (from 1300 to
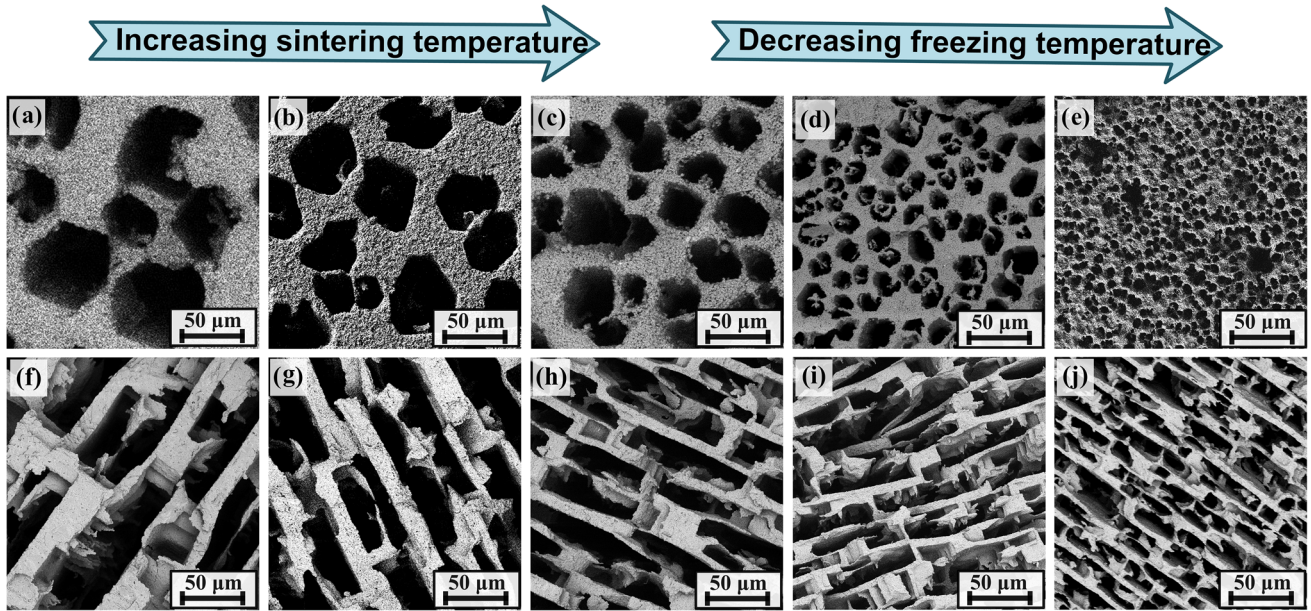
Figure 4 Typical SEM micrographs of porous 1 wt% TiO$_2$-containing alumina prepared from different solvents: **a–e** TBA and **f–j** H$_2$O for different freezing temperatures **a–c**, **f–h** − 10 °C, **d**, **i** − 50 °C and **e**, **j** − 90 °C, and sintering temperatures **a**, **f** 1300 °C, **b**, **g** 1350 °C and **c–e**, **h–j** 1400 °C.

1400 °C), the wall thickness and pore size of the TBA-based samples range from 5 to 41 μm and from 11 to 70 μm, respectively. Meanwhile, those of the water-based samples range from 9 to 32 μm (wall thickness) and from 14 to 43 μm (pore size). Compared with the lamellar structure, the wall thickness and pore size of the honeycomb structure decrease more rapidly either with an increase in sintering temperature or a decrease in freezing temperature. It results from the greater deformation capacity of isotropic honeycomb

Figure 5 Typical wall thickness and pore size distributions of 1 wt% TiO$_2$-containing alumina using different solvents: **a**, **b** TBA and **c**, **d** H$_2$O freeze-cast at temperatures from − 10 to − 90 °C and sintered at temperatures from 1300 to 1400 °C.
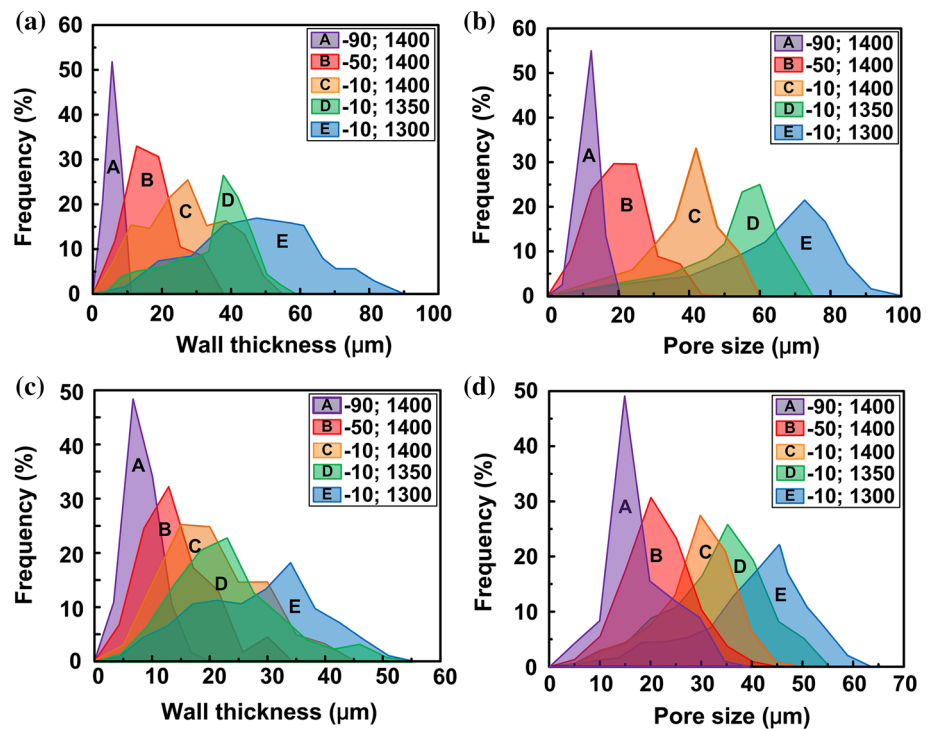
structure and the regional differences in the formation of crystal nuclei and growth mechanisms of TBA and ice crystals. This indicates that the microstructure size of the TBA-based samples is more susceptible to temperature; in other words, they exhibit better structural controllability, which shows greater potential in industry application.

Shrinkage and porosity of the scaffolds

From Fig. 6, we can see the volume of scaffold decreases a lot after sintering. When the solid content is constant, the sintering temperature and freezing temperature are two main parameters controlling the shrinkage and total porosity. Table 1 shows that the line shrinkage and bulk density of two types of scaffolds increase either with the increase in the sintering temperature or the decrease in the freezing temperature. The line shrinkage and bulk density of the scaffolds developed from TBA are higher than those developed from water in all systems with the same freezing and sintering temperatures, which is attributed to the characteristics of pore architecture and the regional differences in the crystallization behavior of TBA and ice crystals. The lamellar pore with a distinct anisotropic characteristic has a greater capacity to resist deformation. In contrast, the ceramic walls in the prismatic structure are connected closely with each other, which offers particles more chance to sinter together. Thus, it favors larger shrinkage of the green bodies.

Figure 7 shows the effect of sintering temperature (1300 °C, 1350 °C and 1400 °C) and freezing
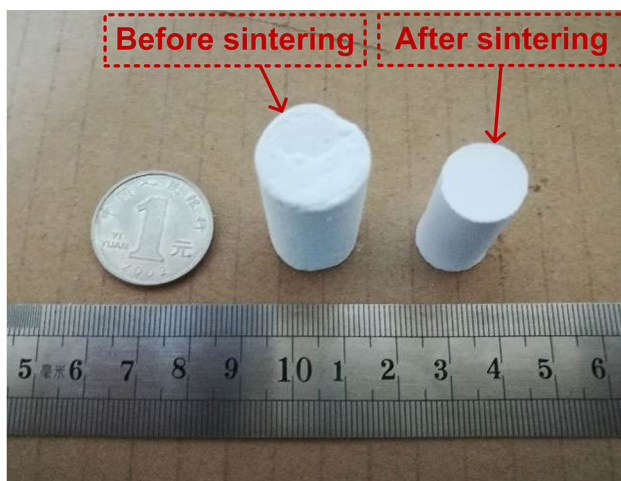

Figure 6 Typical freeze-cast samples before and after sintering.

temperature (− 10 °C, − 50 °C and − 90 °C) on the total porosity of the TBA-based and water-based freeze-cast specimens. The total porosity of the freeze-cast samples reduces with increasing sintering temperature. For example, for the TBA-based scaffolds freeze-cast at − 50 °C, the larger densification of the walls at higher sintering temperatures within the range of 1300–1400 °C drives the larger shrinkage of macropores and therefore the total porosity reduces from 72 to 61%. The total porosity of the TBA-based scaffolds is always 5–10% lower than that of the water-based scaffolds sintered at the same temperature. The reasons for this phenomenon are described as follows: (1) The discrepancy in the solidification volume change: negative (shrinkage) in the case of TBA (− 2%) and positive (expansion) in the case of water (+ 9%). (2) It is known that in freeze casting, particles are rejected by the growing crystals and concentrate in the intercrystals space, until the osmotic pressure exceeds the capillary pressure. At this point, the freezing front starts to engulf the particles. The concentration at which this balance is lost is referred to as the breakthrough concentration which is found to be modified by particle size and surface tension [17]. In our case, compared to the value of pure water, lower surface tension of TBA yields the lower breakthrough concentration. Thus, the greater fraction of micropores processed with TBA makes the densification easier because micropores are easily removed in the green bodies. (3) The lamellar structure with a distinct anisotropic characteristic has a greater capacity to resist deformation, which results in less shrinkage of green bodies and a higher porosity after sintering. Figure 7 also shows that when freezing temperature decreases, the total porosity of the freeze-cast samples decreases slightly. With an increase in the sintering temperature, the effect of freezing temperature on the total porosity became more significant. At the same sintering temperature, the total porosity of the TBA-based scaffolds is more susceptible to the freezing temperature than that of the water-based scaffolds. In general, compared with the sintering temperature, the freezing temperature does not have the same level of effect on the total porosity.

Compressive behavior

Figure 8 shows plots of the average compressive strength of the TBA-based and water-based scaffolds

Table 1 Linear shrinkage and bulk density of TBA-based and water-based alumina scaffolds

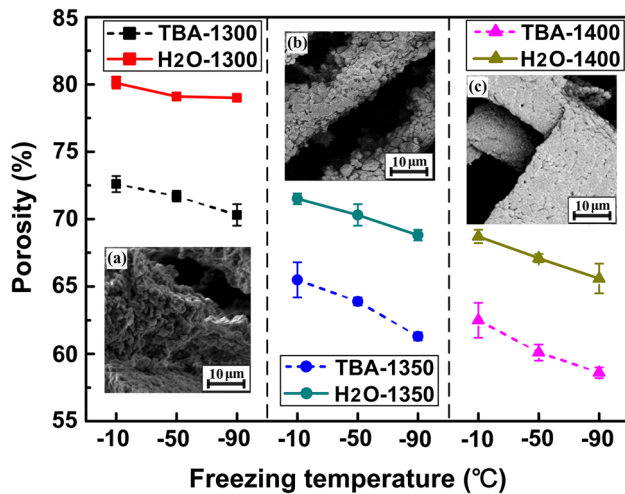| Sintering temperature (°C)	Freezing temperature (°C)	TBA		H₂O	
		Linear shrinkage (%)	Bulk density (g cm⁻³)	Linear shrinkage (%)	Bulk density (g cm⁻³)
1300	− 10	15.6 ± 0.5	1.05 ± 0.04	9.9 ± 0.5	0.79 ± 0.03
	− 50	15.8 ± 0.5	1.11 ± 0.04	10.3 ± 0.7	0.83 ± 0.04
	− 90	16.1 ± 0.6	1.14 ± 0.07	10.4 ± 0.5	0.84 ± 0.02
1350	− 10	19.7 ± 0.6	1.33 ± 0.05	16.4 ± 0.6	1.14 ± 0.04
	− 50	19.9 ± 0.6	1.41 ± 0.06	16.6 ± 0.5	1.16 ± 0.04
	− 90	20.3 ± 0.7	1.44 ± 0.08	17.1 ± 0.6	1.23 ± 0.04
1400	− 10	20.5 ± 0.8	1.43 ± 0.06	16.7 ± 0.5	1.33 ± 0.03
	− 50	22.7 ± 1.1	1.52 ± 0.12	17.7 ± 0.5	1.40 ± 0.04
	− 90	24.0 ± 1.0	1.66 ± 0.11	18.9 ± 0.4	1.44 ± 0.03

Figure 7 Variations of the total porosity with freezing temperature for the TBA-based and water-based freeze-cast alumina samples sintered at different temperatures. The inset images show the evolution of wall densification: (a) water-based ceramic walls sintered at 1300 °C; (b) water-based ceramic walls sintered at 1350 °C; (c) water-based ceramic walls sintered at 1400 °C.

Figure 8 Relationship of the apparent porosity and compressive strength of the TBA-based scaffolds and water-based scaffolds (with typical strain–stress curves showing different fracture behavior observed in two kinds of the scaffolds).

as a function of the total porosity. As indicated, the compressive strength is directly related to the type of pore morphology. The samples with prismatic pores have a higher strength than their counterparts with lamellar pores of similar porosity. As is extensively reported in the literature [25, 26], buckling is the main failure mechanism in the freeze-cast materials. The prismatic pores bring out a specific interworking architecture perpendicular to the load, as shown in Fig. 1a. The necks between prismatic pores are uniformly located and run the length of the sample, as shown in Fig. 1b, while the necks between lamellar
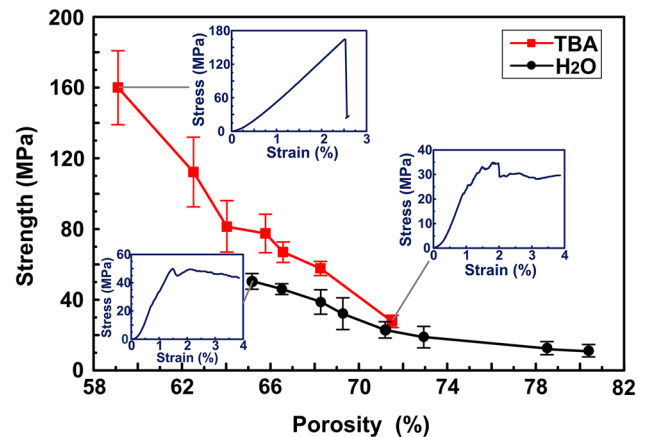
pores are sparse, unevenly located and discontinuous (Fig. 1c, d). The interconnected architecture produced by the prismatic pores remarkably improves the resistance of the scaffolds to local buckling over that of the lamellar pores, which is in accordance with the conclusion of Hunger et al. [26]. This is the main reason for the appreciably higher compressive strength of the TBA-based scaffolds.

On the other hand, the effect of pore morphology on the compressive strength is also influenced by the porosity. For example, for a total porosity of 66%, the compressive strength of 77.9 MPa of the prismatic-structured samples is about 1.8 times that of the lamellar-structured samples (44.5 MPa). In contrast, when the total porosity reaches 72%, the former (23.8 MPa) is nearly 1.1 times that of the latter (21.5 MPa). It suggests that the lager porosity
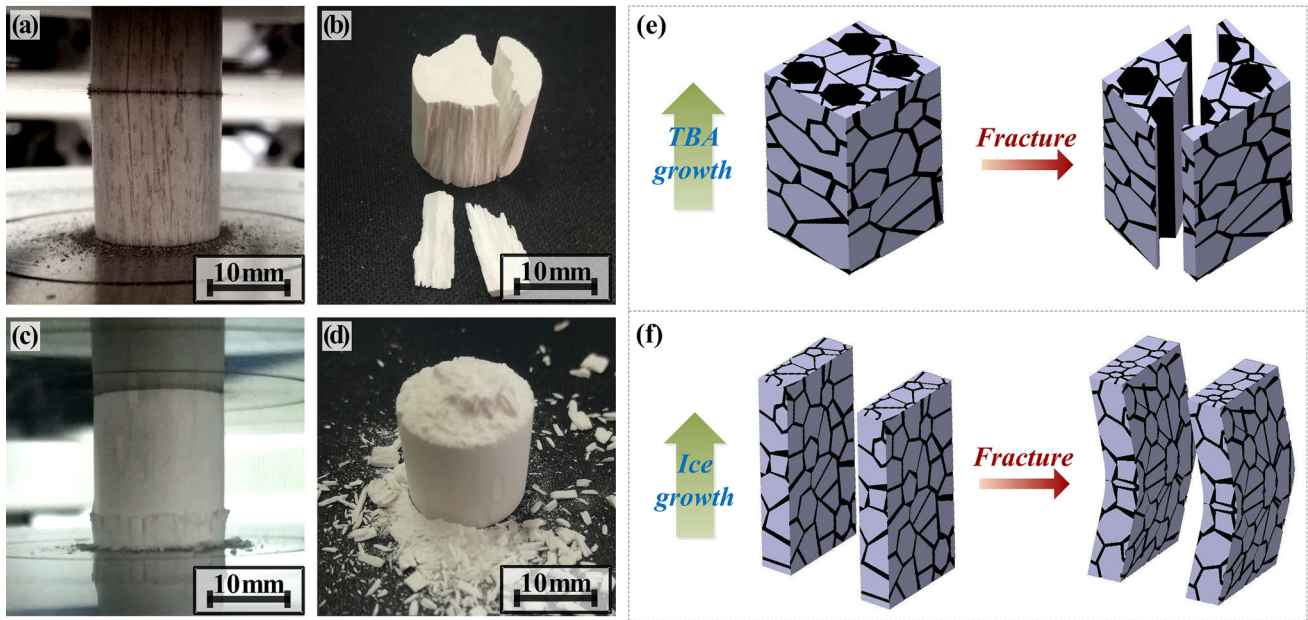
Figure 9 a, b Close-ups of the sudden rupture sample (TBA-based scaffold freeze-cast at − 90 °C and sintered at 1400 °C) and **c, d** the progressive crushing sample (water-based scaffold freeze-cast at − 90 °C and sintered at 1400 °C); fracture modes of **e** honeycomb structures and **f** lamellar structures.

weakens the effect of the pore morphology on the compressive strength. This noticeable reduction in the strength might be related to the increase in microstructural defects observed in the scaffolds with a larger porosity obtained by decreasing the sintering temperature. The formation of weaker necks between particles results in the loss of the anti-buckling capacity of the TBA-based scaffolds.

An interesting phenomenon that can be observed from the typical strain–stress curves in Fig. 8 is that the failure behavior of the TBA-based samples changes from a sudden rupture to progressive crushing with increasing total porosity. The TBA-based scaffolds with a total porosity of lower than 68% present the sudden rupture and those with a total porosity larger than 68% present the progressive crushing behavior. Although it is a kind of brittle fracture, the strain–stress curves of the progressively crushed samples are similar to those of plastic materials, which show relatively low strength but strong ability to maintain a loading capacity in the case of local failure. The main cause of this behavior is that the relatively high porosity and incompact ceramic walls are disadvantageous to stress transmission. When the most vulnerable walls of the scaffold reach the load capacity limit, local buckling occurs, which causes the rest of the walls to undertake a larger load. Hence, the sample tends to fail

progressively. In contrast, the dense walls result in good stress transmission. The load distribution on the walls is uniform and the stress concentration is reduced. Furthermore, there are no clearly vulnerable walls. The extra effect of low porosity on the compressive strength of porous ceramics is a decrease in crack growth, which creates a highly cranky pathway and a corresponding increase in the dissipation energy during crack propagation. Therefore, when the load limit is reached, the material fails in a sudden rupture with one or several long cracks. Different from the TBA-based scaffolds, in this work, no sudden rupture is observed in the water-based scaffolds (with a total porosity of 65–81%). Rupture would occur at a lower stress, demonstrating that the lamellar structures are more likely to fail progressively than the honeycomb structures. This trend is related not only to the possibility of crack formation and growth due to local buckling of ceramic walls but also to the evenness of load distribution in the ceramic walls. The ceramic walls of the lamellar structures are nearly isolated, which is poor for stress transmission. But in prismatic structures, walls are all connected and able to support each other under the compression forces. Moreover, prismatic pores make crack deflected during propagation, yielding higher compressive properties. In response to the compressive loading, honeycomb structures prevent Euler
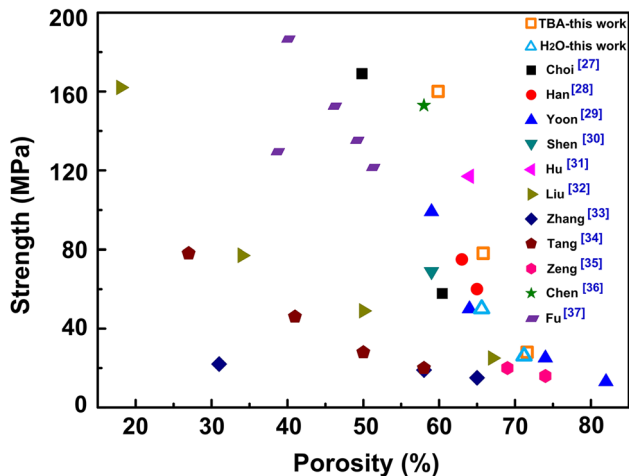
Figure 10 Comparison of the maximum compressive strength of the alumina scaffolds prepared by directional freeze casting as a function of porosity from the literature data and the present work [27–37].

buckling by offering mutual restriction and hindering crack propagation through ceramic walls. Figure 9 shows the typical fracture behavior observed in two kinds of the scaffolds and the schematic fracture models built through CATIA software.

Figure 10 presents a comparison of the maximum compressive strength of the alumina scaffolds achieved by directional freeze casting as a function of porosity from the literature data together with some of the present work. The data in the literature vary greatly. The compressive strength of the freeze-cast alumina is essentially dependent on the total pore volume. In general, the compressive strength of the scaffolds fabricated in this work is within the scope of the literature data. However, it is worth noting that the value of 160 MPa obtained from the TBA-based scaffolds with 59% porosity (freeze-cast at − 90 °C and sintered at 1400 °C) is higher than the values reported in the literature, suggesting a prominent strengthening effect of the TiO_2 sintering aids and prismatic pore morphology.

Conclusions

Directionally aligned prismatic and lamellar porous Al_2O_3 with dense ceramic walls were successfully fabricated from submicron Al_2O_3 powders and a tiny quantity of (1 wt%) nanoscale TiO_2 by freeze casting using TBA and water as templates, respectively. By changing freezing temperature and sintering

temperature, honeycomb-structured Al_2O_3 with low density (1.05–1.66 g cm^{-3}), high compressive strength (23.8–160 MPa), controllable pore size (11–70 μm) and wall thickness (5–41 μm) have been prepared. Compared to the water-based samples, the TBA-based Al_2O_3 is characterized by larger shrinkage after sintering (about 5.5% larger), lower porosity (5–10% lower), better controllability of pore dimension (103% broader) and wall thickness (57% broader) and superior compressive strength (10–80% higher at the same porosity). Different failure modes observed between the TBA-based samples and the water-based samples reveal that the honeycomb structures are more likely to fail suddenly than the lamellar structures. In addition, a high strength-to-density ratio of up to 160 MPa/1.66 g cm^{-3} was achieved in the TBA-based porous Al_2O_3 scaffold suggesting prominent strengthening effects resulting from the TiO_2 sintering aids and prismatic pore morphology.

Acknowledgements

References

[1] Colombo P (2008) In praise of pores. Science 322:381–383

[2] Green DJ, Colombo P (2003) Cellular ceramics: intriguing structures, novel properties, and innovative applications. MRS Bull 28:296–300

[3] Souza DF, Nunes EHM, Pimenta DS, Vasconcelos DCL, Nascimento JF, Grava W, Houmard M, Vasconcelos WL (2014) Synthesis and structural evaluation of freeze-cast porous alumina. Mater Charact 96:183–195

[4] Hollister SJ (2005) Porous scaffold design for tissue engineering. Nat Mater 4:518–524

[5] Li Y, Fu ZY, Su BL (2012) Hierarchically structured porous materials for energy conversion and storage. Adv Funct Mater 22:4634–4667

[6] Han YS, Li JB, Chen YJ (2003) Fabrication of bimodal porous ceramics. Mater Res Bull 38:373–379

[7] Boaro M, Vohs JM, Gorte RJ (2003) Synthesis of highly porous yttria-stabilized zirconia by tape-casting methods. J Am Ceram Soc 86:395–400

[8] Sarhadi F, Afarani MS, Kalhori DM, Shayesteh M (2016) Fabrication of alumina porous scaffolds with aligned oriented pores for bone tissue engineering applications. Appl Phys A 122:1–8

[9] Isobe T, Kameshima Y, Nakajima A, Okada K (2007) Preparation and properties of porous alumina ceramics with unidirectionally oriented pores by extrusion method using a plastic substance as a pore former. J Eur Ceram Soc 27:61–66

[10] Deville S, Saiz E, Nalla RK, Tomsia AP (2006) Freezing as a path to build complex composites. Science 311:515–518

[11] Deville S, Saiz E, Tomsia AP (2006) Freeze casting of hydroxyapatite scaffolds for bone tissue engineering. Biomaterials 27:5480–5489

[12] Deville S (2008) Freeze-casting of porous ceramics: a review of current achievements and issues. Adv Eng Mater 10:155–169

[13] Xu TT, Wang CA (2016) Control of pore size and wall thickness of 3-1 type porous PZT ceramics during freeze-casting process. Mater Des 91:242–247

[14] Wang Z, Feng P, Wang X, Geng P, Akhtar F, Zhang HF (2016) Fabrication and properties of freeze-cast mullite foams derived from coal-series kaolin. Ceram Int 42:12414–12421

[15] Guizard C, Leloup J, Deville S (2014) Crystal templating with mutually miscible solvents: a simple path to hierarchical porosity. J Am Ceram Soc 97:2020–2023

[16] Deville S, Saiz E, Tomsia AP (2007) Ice-templated porous alumina structures. Acta Mater 55:1965–1974

[17] Deville S, Bernard-Granger G (2011) Influence of surface tension, osmotic pressure and pores morphology on the densification of ice-templated ceramics. J Eur Ceram Soc 31:983–987

[18] Tang Y, Qiu S, Wu C, Miao Q, Zhao K (2016) Freeze cast fabrication of porous ceramics using tert-butyl alcohol-water crystals as template. J Eur Ceram Soc 36:1513–1518

[19] Liu R, Yuan J, Wang CA (2013) A novel way to fabricate tubular porous mullite membrane supports by TBA-based freezing casting method. J Eur Ceram Soc 33:3249–3256

[20] Smothers WJ, Reynolds HJ (1954) Sintering and grain growth of alumina. J Am Ceram Soc 37:588–594

[21] Bagley RD, Cutler IB, Johnson DL (1970) Effect of TiO_2 on initial sintering of Al_2O_3. J Am Ceram Soc 53:136–141

[22] Silva AMA, Nunes EHM, Souza DF, Martens DL, Diniz da Costab JC, Houmard M, Vasconcelos WL (2015) Effect of titania addition on the properties of freeze-cast alumina samples. Ceram Int 41:10467–10475

[23] Kebbede A, Parai J, Carim AH (2000) Anisotropic grain growth in α-Al_2O_3 with SiO_2 and TiO_2 additions. J Am Ceram Soc 83:2845–2851

[24] Bueno S, Hernández MG, Sánchez T, Anaya JJ, Baudín C (2008) Non-destructive characterisation of alumina/aluminium titanate composites using a micromechanical model and ultrasonic determinations: part I. Evaluation of the effective elastic constants of aluminium titanate. Ceram Int 34:181–188

[25] Ojuva A, Järveläinen M, Bauer M, Keskinen L, Valkonen M, Akhtar F, Leväne E, Bergström L (2015) Mechanical performance and CO_2 uptake of ion-exchanged zeolite A structured by freeze-casting. J Eur Ceram Soc 35:2607–2618

[26] Hunger PM, Donius AE, Wegst UGK (2013) Structure-property-processing correlations in freeze-cast composite scaffolds. Acta Biomater 9:6338–6348

[27] Choi HJ, Yang TY, Yoon SY, Kim BK, Park HC (2012) Porous alumina/zirconia layered composites with unidirectional pore channels processed using a tertiary-butyl alcohol-based freeze casting. Mater Chem Phys 133:16–20

[28] Han JC, Hu LY, Zhang YM (2009) Fabrication of ceramics with complex porous structures by the impregnate-freeze-casting process. J Am Ceram Soc 92:2165–2167

[29] Yoon BH, Choi WY, Kim HE, Kim JH, Koh YH (2008) Aligned porous alumina ceramics with high compressive strengths for bone tissue engineering. Scr Mater 58:537–540

[30] Shen P, Xi JW, Fu YJ, Shaga A, Sun C, Jiang QC (2014) Preparation of high-strength Al–Mg–Si/Al_2O_3 composites with lamellar structures using freeze casting and pressureless infiltration techniques. Acta Metall Sin (Engl Lett) 27:944–950

[31] Hu LY, Zhang YM, Dong SL, Zhang SM, Li BX (2013) In situ growth of hydroxyapatite on lamellar alumina scaffolds with aligned pore channels. Ceram Int 39:6287–6291

[32] Liu G, Zhang D, Meggs C, Button TW (2010) Porous Al_2O_3–ZrO_2 composites fabricated by an ice template method. Scr Mater 62:466–468

[33] Zhang D, Zhang Y, Xie R, Zhou KC (2012) Freeze gel-casting of aqueous alumina suspensions for porous ceramics. Ceram Int 38:6063–6066

[34] Tang YF, Miao Q, Qiu S, Zhao K, Hu L (2014) Novel freeze-casting fabrication of aligned lamellar porous alumina with a centrosymmetric structure. J Eur Ceram Soc 34:4077–4082

[35] Zeng J, Zhang Y, Zhou K, Zhang D (2014) Effects of alcohol additives on pore structure and morphology of freeze-cast ceramics. Trans Nonferrous Met Soc China 24:718–722

[36] Chen RF, Wang CA, Huang Y, Ma LG, Lin WY (2007) Ceramics with special porous structures fabricated by freeze-gelcasting: using tert-butyl alcohol as a template. J Am Ceram Soc 90:3478–3484

[37] Fu YJ, Shen P, Hu ZJ, Sun C, Guo RF, Jiang QC (2016) The role of CuO–TiO_2 additives in the preparation of high-strength porous alumina scaffolds using directional freeze casting. J Porous Mater 23:539–547